

High-Density Arrays of InGaN Nanorings, Nanodots, and Nanoarrows Fabricated by a Template-Assisted Approach

Yadong Wang,^{*,†} Keyan Zang,^{†,‡} Soojin Chua,^{*,†,‡} Melissa S. Sander,^{‡,§}
Sudhiranjan Tripathy,[‡] and Clifton G. Fonstad^{†,⊥}

Singapore-MIT Alliance, E4-04-10, 4 Engineering Drive 3, Singapore 117576, Institute of Materials Research and Engineering, 3 Research Link, Singapore 117602, and Department of Electrical and Computer Science, Massachusetts Institute of Technology, Cambridge, Massachusetts 02139

Received: January 20, 2006; In Final Form: April 7, 2006

Dense, crystalline arrays of InGaN nanorings, nanodots, and nanoarrows have been fabricated on GaN substrates by template-assisted nano-area selective growth. To create the nanostructures, we have used nanoporous anodic alumina films as templates to pattern nanopores in an SiO₂ transfer layer, and then used this patterned SiO₂ layer as a template for nitride growth by metalorganic chemical vapor deposition. We have varied the diameter of the deposited nitride nanostructures from 35 to 250 nm by changing the initial anodic alumina template structure. In addition, by controlling the nitride growth time we have created various types of nanostructures, from nanorings to nanoarrows. This structural evolution begins with the nucleation and formation of a nanoring structure, followed by coalescence and growth to form faceted nanodots, and finally lateral overgrowth to form faceted nanoarrows.

1. Introduction

Group III nitride semiconductors are presently the subject of intense research due to their applicability in short wavelength optoelectronics and high power electronics. The commercial availability of III-nitride-based super-bright blue and green light emitting diodes (LEDs) and blue/UV laser diodes (LDs) is a clear indication of the great potential of this material system.^{1–3} In particular, significant work has been reported on nitride nanostructure fabrication. This work is partially driven by an expected decrease in the threshold current temperature dependence in nanostructures as compared to the bulk.⁴

Several approaches have been employed to fabricate nitride nanostructures. Conventional Stranski–Krastanow (S-K) growth has been used for the formation of (In)GaN quantum dots (QDs) by molecular beam epitaxy (MBE), where the epitaxial growth of (In)GaN exhibits a 2D–3D growth transition.⁵ The self-assembled formation of (In)GaN QDs has also been reported by using silicon as an antisurfactant for growth on AlGaIn surfaces.⁶ Producing nanodots with the S-K growth mode normally results in a random distribution of dots. The diameters of the dots and the spacing between the dots are not well-controlled, which is a limitation for device applications. Recently, InGaN nanodots have been fabricated by the selective growth of GaN micropillar arrays topped with InGaN/GaN quantum wells.^{7,8} The GaN pillars were formed by metal–organic chemical vapor deposition of GaN through an array of circular holes with diameters of a few micrometers, which were lithographically patterned in a silica mask on a GaN-on-sapphire substrate. This technique enables precise control of the position of the features; however, the low nanostructure density limits

the usefulness of these structures for practical device applications. Nanostructures have also been created by deposition into patterned substrates produced by conventional lithographic approaches, such as e-beam lithography, interference lithography, or X-ray lithography. For example, arrays of uniform InAs, InGaAs, and Ge nanodots have been fabricated by combining nanoscale lithographic patterning and selective growth.^{9–11} In addition, Lachab et al. have demonstrated the fabrication of InGaN nanostructures by selective growth on Si-coated GaN/sapphire substrates using focused ion beam lithography and MOCVD.¹² While lithographic approaches enable precise control of the spacing and position of nanofeatures, these techniques are typically limited by high cost and low throughput. Therefore, it is of interest to develop new approaches that can be used to fabricate dense arrays of nanostructures over large areas on substrates with more practical, higher throughput approaches.

Patterning based on self-organization processes offers a number of advantages for fabricating arrays of nanostructures as compared to typical lithographic patterning approaches, including the ability to pattern nanoscale features over large areas simultaneously, relative process simplicity, and low cost. In particular, self-ordered nanoporous anodic aluminum oxide (AAO) templates are easily produced, versatile structures for fabricating semiconductor nanostructure arrays.^{13–17} AAO is created by the anodization of aluminum and is composed of ordered arrays of tunable diameter pores ranging from ~3 to 500 nm.^{18–23} We have recently reported the fabrication of dense arrays of 75 nm InGaN nanodots and nanorings on GaN by MOCVD through an SiO₂ transfer layer using AAO as a mask, and Deb et al. have used a similar approach to create ~100 and ~50 nm GaN nanorod arrays.^{24,25} Here we describe in detail our ability to control nanostructure formation in order to fabricate a range of InGaN nanostructures using AAO template-assisted nano-area selective growth. We have demonstrated that not only the size but also the shape of the nanostructures can

* Address correspondence to these authors. E-mail: Y. D.W., smap1018@nus.edu.sg; S.J.C., elecsj@nus.edu.sg.

[†] Singapore-MIT Alliance.

[‡] Institute of Materials Research and Engineering.

[§] Current address: GE Global Research, Niskayuna, NY 12309.

[⊥] Massachusetts Institute of Technology.

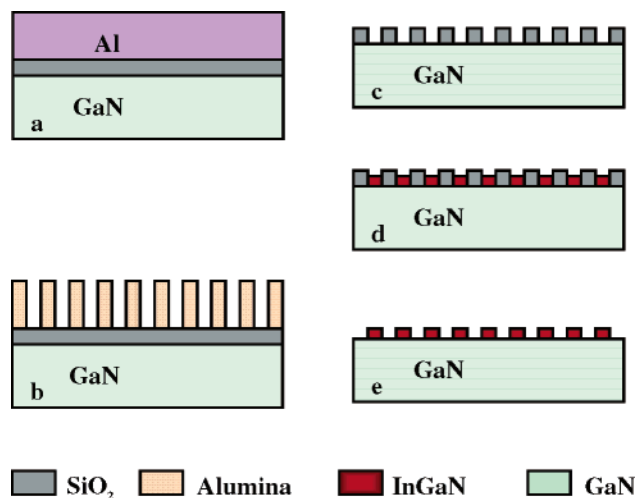


Figure 1. Schematic of the process used to fabricate a dense array of InGaN nanostructures: (a) a thin SiO₂ film is grown on an as-grown GaN layer, followed by evaporation of a 1 μ m thick aluminum film, (b) an \sim 100–300 nm thick ordered AAO template is fabricated with a two-step anodization process, (c) CF₄-based ICP etching is used to transfer the nanopores from AAO to SiO₂, followed by removal of the AAO template, (d) an InGaN nanostructure array is grown by MOCVD through the nanopores of SiO₂, and (e) SiO₂ is removed in dilute HF to reveal the InGaN nanostructure array on the GaN substrate.

be controlled by tuning the AAO template dimensions and nanostructure growth conditions.

2. Experimental Sections

The general procedure to produce dense InGaN nanostructures is shown schematically in Figure 1. The first step is to grow a conventional low-temperature GaN nucleation layer on a sapphire (0001) substrate, followed by the deposition of 1.5–2 μ m of GaN at 1050 $^{\circ}$ C with MOCVD. The surface of the as-grown GaN epilayer shows steplike morphology and the rms surface roughness of the epilayer is \sim 0.4 nm. A relatively smooth surface of the starting epilayer is necessary to enable good control over the following processing steps for template fabrication. Next, a thin layer of SiO₂ (\sim 100 nm) is deposited on the top of GaN by plasma enhanced chemical vapor deposition (PECVD), followed by evaporation of 1 μ m of aluminum onto the substrate (Figure 1a). Then the aluminum film is anodized with a two-step anodization process. The two-step anodization involves first anodizing the Al film part way, then removing the alumina layer that has been formed and anodizing the remaining Al in a second process. Anodization is conducted under constant voltage in either sulfuric, oxalic, or phosphoric acid, depending on the desired pore diameter and spacing. The substrates are mounted on copper plates for the anodization. During the anodization, the electrolyte is vigorously stirred and the temperature kept at \sim 2 $^{\circ}$ C. After complete anodization, the thin barrier layer at the bottom of the pores is removed and the pores are widened by immersing the samples in 5 wt % H₃PO₄ for 30–150 min depending on the desired pore size. To transfer the nanopores from the AAO template to the SiO₂ film (as shown in Figure 1c), CF₄-based inductively coupled plasma (ICP) etching is employed. ICP etching is carried out in a load-locked Plasma-Therm SLR-770 setup with 2.0 MHz source configured with an electrode chuck in the chamber, which is biased separately at 13.56 MHz. The patterned samples are exposed to a CF₄/He plasma. The flow rates of CF₄ and He are both 20 sccm. The operating pressure is kept constant at 10 mTorr during etching. The inductive power

is kept at 500 W at a constant rf chuck power of 80 W. After pattern transfer to the SiO₂ layer, the AAO template is selectively etched away in 5 wt % phosphoric acid. Prior to the nitride regrowth, samples are immersed in acetone and rinsed in DI water to remove organic contaminants. Then the patterned samples are dipped in a buffer HCl solution to remove the surface oxide from the underlying GaN layer. Nanostructures are then deposited through the nanoporous SiO₂ template by MOCVD (Figure 1d). The nanopatterned sample is first annealed in an N₂ ambient for 2 min at 1020 $^{\circ}$ C in the MOCVD reactor to remove any surface damage caused by ICP etching. Then the growth temperature is reduced to 750 $^{\circ}$ C for InGaN growth. Trimethylgallium (TMGa) and trimethylindium (TMIn) are used as group III sources and NH₃ as the group V source. N₂ is used as a carrier gas. The growth pressure is kept at 100 Torr. The growth time varies from 1 min to 12 min depending on the nanopore size and desired nanostructure morphology. The In composition target is set at 5–10%. After growth, the SiO₂ template is removed with a dilute HF solution, revealing the well-ordered nanostructure arrays (Figure 1e). SEM (JEOL 6700FESEM), AFM (Digital Nanoscope III AFM), and TEM (Phillips EM 300 TEM) were used to assess the structures. Low photoluminescence measurements were performed in a helium close-cycle cryostat. The 325 nm line of the He–Cd laser was used as the source of excitation.

3. Results and Discussion

3.1. Template Fabrication and Pattern Transfer. Figure 2a–c shows SEM images of porous anodic alumina templates with different pore spacings and pore diameters created by anodization at different potentials. The diameters of the pores are \sim 35, 65, and 150 nm, and were created with the following anodization conditions: 0.2 M sulfuric acid at 25 V with 35 min pore widening; 0.3 M oxalic acid at 40 V with 65 min pore widening; and 0.3 M phosphoric acid at 150 V with 120 min pore widening, respectively. It has been reported that 0.15–0.5 μ m thick AAO templates are necessary for effective nanopore pattern transfer during plasma etching.^{13,14} We employed a two-step anodization of the 1 μ m thick Al films in order to obtain templates that are thin enough ($<$ 500 nm) to enable good transfer of the pore patterns from the alumina template to the SiO₂ layer. In addition, by using a two-step anodization process at suitable anodization conditions, it is possible to obtain more ordered, uniform diameter pores.¹⁸ The diameter of the pores can be tuned over a wide range by controlling the anodization voltage and post-anodization etching time.²⁶ Because our starting aluminum thickness is only \sim 1 μ m, the pores do not have long-range hexagonal ordering. Since the pores tend to form first at random defects on the aluminum surface and become more ordered as the pores grow in length, the degree of ordering can be increased by starting with thicker films or patterning the initial aluminum film prior to the pore formation by using a mold.^{27,28}

CF₄-based inductively coupled plasma (ICP) etching was employed to transfer the pore pattern from the AAO template to the underlying SiO₂. The SiO₂ was etched for approximately 1–2 min to expose the underlying GaN layer. By using low power and a short etching time, etching of the GaN surface is minimized, and any damage that does occur can be reduced by a high-temperature annealing step in the MOCVD growth chamber, as described above. Figure 3 shows an SEM image of the pore patterns in the SiO₂ layer on the GaN surface after the AAO template has been partially removed. In this example, the AAO template was produced by anodization of Al in

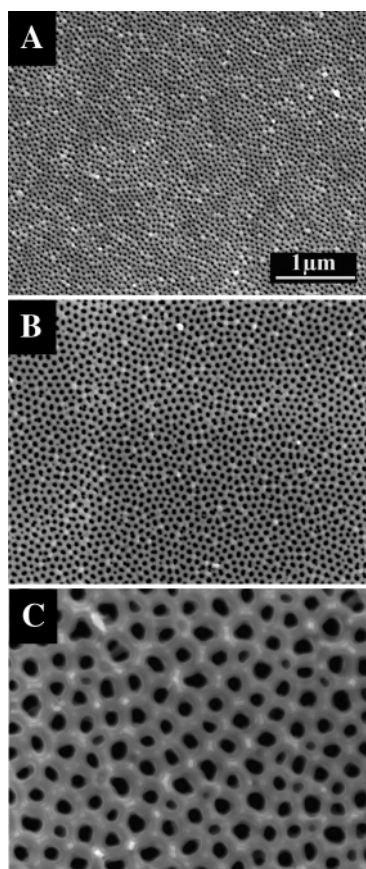


Figure 2. SEM images of the AAO templates with different pore diameters and interpore distances corresponding to the different anodization conditions: (a) 0.2 M sulfuric acid at 25 V with 35 min pore-widening treatment; (b) 0.3 M oxalic acid at 40 V with 65 min pore-widening treatment; and (c) 0.3 M phosphoric acid at 150 V with 120 min pore-widening treatment.

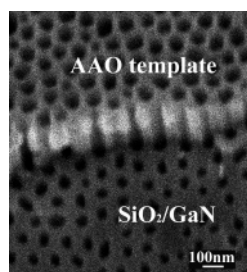


Figure 3. SEM image of nanopores in SiO₂ as transferred by ICP etching from the AAO template; the AAO template has been partially removed.

0.3 M oxalic acid at 40 V with a 60 min pore-widening treatment in 5 wt % phosphoric acid. The average diameter of the pores is ~ 60 nm. It is clear that the diameter and the periodicity of the nanopores in the SiO₂ have been directly transferred from the AAO template.

3.2. InGaN Nanodot Array Fabrication. Figure 4 shows an SEM image of an InGaN nanodot array with the SiO₂ mask still in place. The growth temperature and pressure during InGaN growth are kept at 750 °C and 100 Torr. The growth time for this sample was 5 min. The diameter and periodicity of the InGaN nanodots in the array correlate well with those of the nanopores in SiO₂. This image shows that the InGaN dots grow selectively in the pores of the SiO₂, and no significant InGaN nucleation occurs on the SiO₂ surface. It is well established that SiO₂ is an effective mask material for nitride MOCVD growth.^{29,30} The InGaN growth mechanism is expected to be

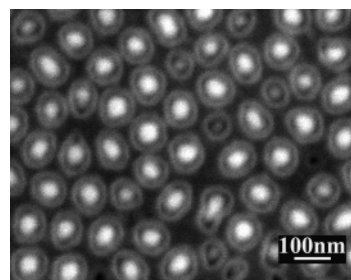


Figure 4. SEM image of the InGaN nanodot array with the SiO₂ mask intact.

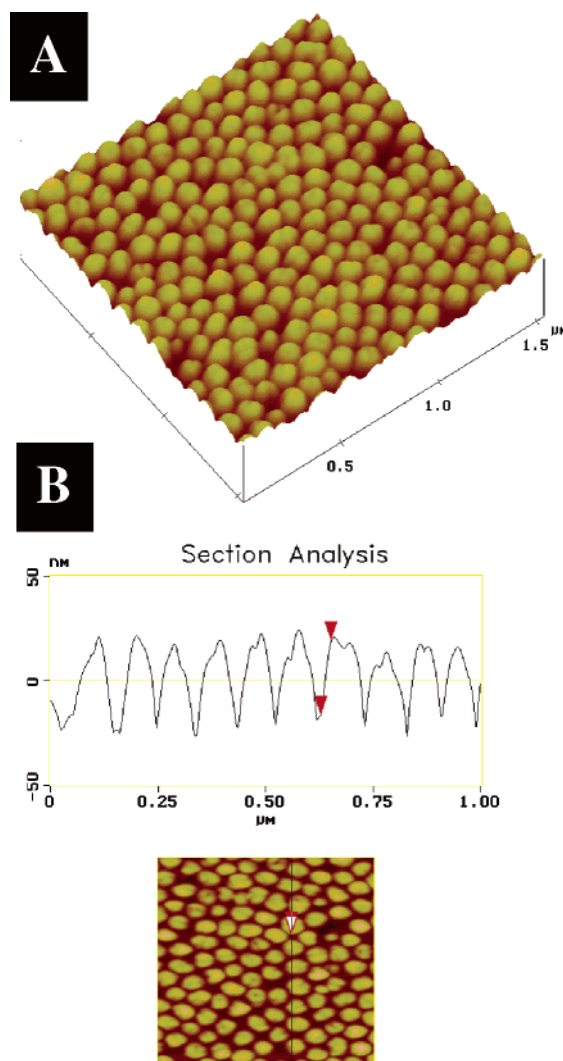


Figure 5. AFM image of the InGaN nanodot arrays: (a) 3D view and (b) sectional view.

similar to the initial stage of epitaxial lateral overgrowth (ELO).³¹ In this case, the InGaN grows selectively on the exposed GaN substrate rather than on the surrounding SiO₂ mask due to the much higher sticking coefficient of group III adatoms on the GaN surface than on the SiO₂.

Figure 5 shows an AFM image of an InGaN nanodot array after the SiO₂ has been removed with a dilute HF solution. The density of the dots is $\sim 10^{10}/\text{cm}^2$. The diameter and height of the dots in this array are 60 ± 5 and 45 ± 5 nm, respectively. By controlling the AAO template parameters it is possible to tune the nanopore pattern in the SiO₂, which enables the formation of InGaN nanodots with different diameters. Figure 6a–c shows SEM images of InGaN nanodot arrays with average

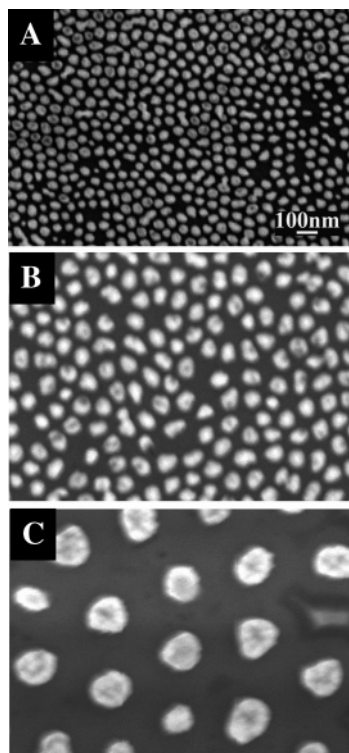


Figure 6. SEM images of the InGaN nanodot arrays with different average dot diameters: (a) 35, (b) 65, and (c) 150 nm.

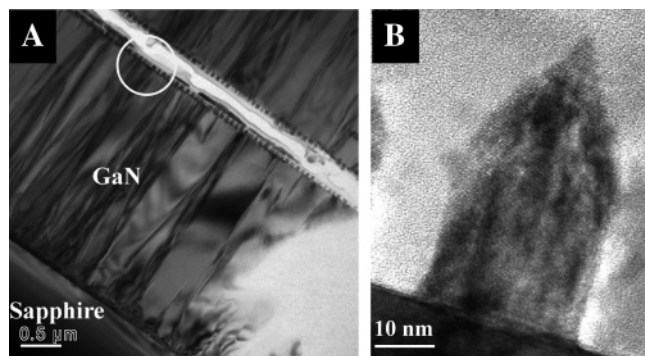


Figure 7. (a) Cross-sectional TEM of the dense InGaN nanodot arrays on GaN substrate; (b) high-resolution TEM image of an individual InGaN nanodot.

diameters of 35, 65, and 150 nm, respectively, after removing the SiO₂ mask. The anodization conditions for the AAO template are the same as described in Figure 2. The growth times for these three samples were 3, 5, and 5 min, respectively.

Figure 7a shows a low magnification TEM image of an InGaN nanodot array with an average dot diameter of ~35 nm. The InGaN nanodots are dense and uniform across the surface of the 2 μm thick underlying GaN layer. It is important to note that many of dislocations in the underlying GaN are blocked by the SiO₂ and cannot propagate to the nanodots. Because the average distance between two dislocation lines in the GaN is on the scale of 100 nm, and the diameter of the nanodots is ~35 nm, there is a low likelihood for preexisting threading dislocations in the underlying GaN to propagate through to the dots. A TEM image of an individual InGaN nanodot is shown in Figure 7b. The InGaN nanodot has a faceted structure, which is consistent with being a hexagonal pyramid bounded by {1101} facets. This structure is energetically stable and has been observed in microscale feature growth.^{32,33} Deb et al. have also

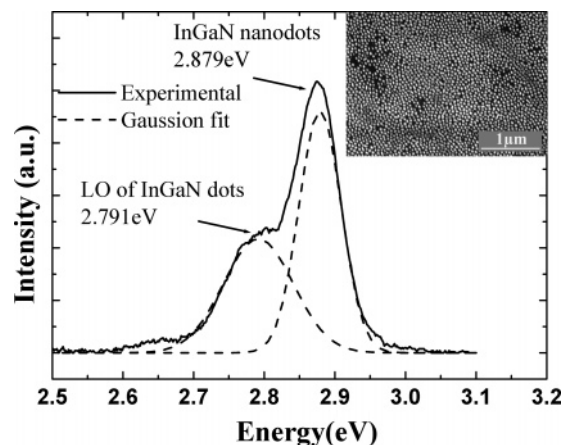


Figure 8. PL spectrum of InGaN nanodot arrays capped with 10 nm GaN with a diameter of 35 nm.

shown that selectively grown GaN nanorods have this structure.²⁵

3.3. Optical Properties of InGaN Nanodot Arrays. Figure 8 shows the PL spectrum at 10 K of ~35 nm diameter InGaN nanodots capped with a 10 nm GaN layer. The growth temperature of the GaN capping layer was the same as that of the InGaN dots. The morphology of the InGaN/GaN nanodot array is shown in the SEM image in the inset of Figure 8. A strong emission peak at 2.879 eV was clearly observed from the InGaN nanodots. The emission peak at 2.791 eV is attributed to the LO phonon replica of InGaN dots, which is ~88 meV lower energy than the main peak. In contrast to the S-K growth model, there is no wetting layer in this InGaN nanodot growth, as confirmed by cross-sectional TEM. A similar morphology was also observed by Mei et al., when they grew InGaAs nanodots on the GaAs substrate from a mask.³⁴ The fwhm of the emission peak from the InGaN dots is only 55 meV, which is narrower than that of InGaN dots grown by the S-K method.³⁵ Typically, the fwhm of dots is strongly dependent on the distribution of the size of the nanostructures. The narrow width of the emission peak is indicative of the good size uniformity of the dots in the array, and this is also consistent with the SEM results. Another important feature about the PL spectrum is that the luminescent peak from the InGaN nanodots is blue shifted as compared with that of an InGaN/GaN single quantum well (3.06 eV) grown on a flat GaN substrate with the same growth conditions (not shown here). A probable cause for the blue shift is incorporation of more In into the nanostructures than in the thin film. According to the Luryi and Suhir model,³⁶ the strain energy density decays exponentially from the heterojunction in the nanoscale growth window. In addition, Alizadeh's simulation work proposed that the misfit-induced strain effects in InGaN are negligible for nanoscale selective growth.³⁷ During the growth of two-dimensional InGaN thin films on GaN, the compressive strain often hinders the incorporation of In atoms into the InGaN lattice. However, in the case of InGaN quantum dots or nanoparticles, the reduced strain may allow more In atoms to be incorporated into the lattice.

3.4. Structure Evolution during Nanostructure Selective Growth. To investigate the growth mechanism in more detail, three InGaN samples have been grown on nanopatterned SiO₂/GaN substrates for different growth times with the same starting SiO₂ template dimensions. The growth times for the three samples were 1, 5, and 12 min, respectively. The thickness of the SiO₂ for the three samples was ~100 nm. The AAO templates were produced in 0.3 M oxalic acid at 40 V with

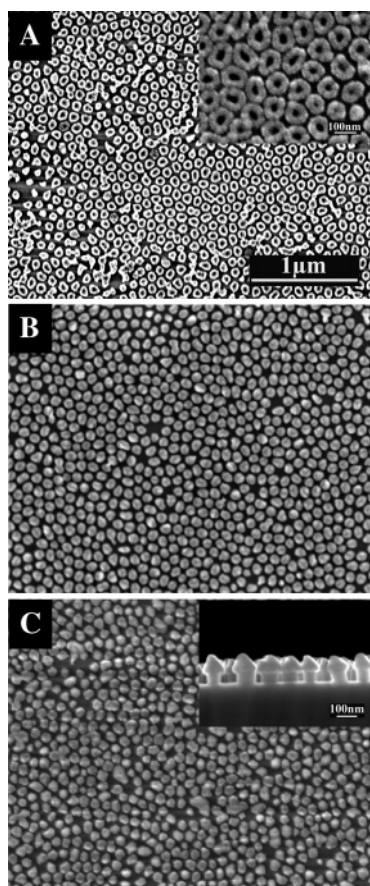


Figure 9. SEM images of InGaN nanostructures: (a) nanorings (inset shows the larger magnitude); (b) nanodots; and (c) nanoarrows (inset shows the cross-sectional view).

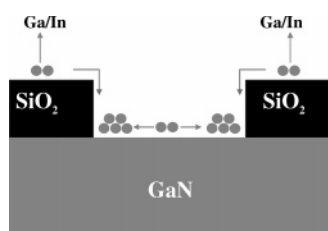


Figure 10. Schematic diagram of atoms migration in the initial growth.

75 min of pore-widening. The resulting average pore diameter in the AAO template is ~ 75 nm. Figure 9 shows SEM images of the three InGaN samples with different growth times. We have observed that initial growth in the nanoporous SiO_2 occurs at the bottom edge of the openings and results in nanorings as shown in Figure 9a. The outer diameter of rings is around 75 nm, which is the same as the pore diameter in the SiO_2 layer. The mean inner diameter of rings is 30 nm as seen in the higher magnification image of the rings in the Figure 9a inset. The edges of the masks are expected to be potential nucleation sites during the growth due to lower nucleation energy, so that the InGaN nucleates and grows first at the edges of the pores. As discussed in the above section, there is no observed deposition on the surface of the SiO_2 mask. The depositing adatoms (depicted as Ga and In in Figure 10) cannot adhere to the SiO_2 surface and must either evaporate or migrate and diffuse along the surface to the nanopores in the SiO_2 . This process during InGaN growth creates an additional supply of active species that can be transported via diffusion to the nanopore areas. In the initial growth stages, the source gas concentration becomes high at the edge region because of this lateral diffusion. Kato

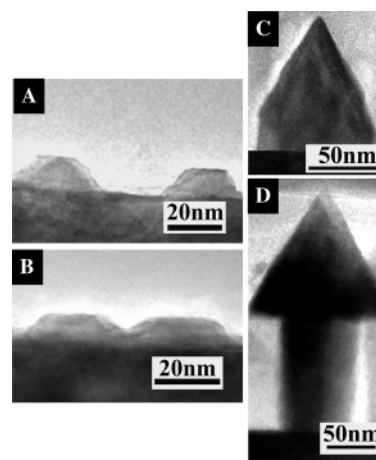


Figure 11. High-resolution TEM images of individual InGaN nanostructures: (a and b) nanorings; (c) nanodots; and (d) nanoarrows.

et al. have also observed the formation of ridge growth at the edge of their $50\text{-}\mu\text{m}$ windows, which is attributed to this lateral vapor phase diffusion of the source gas flowing from the mask region to the window region.³⁸ In addition, from a classical thermodynamics view, the edges of the mask can serve as heterogeneous nucleation centers. The activation energy barrier for heterogeneous nucleation is smaller than that for homogeneous nucleation.³⁹ Therefore, nucleation occurs more readily at steps, and near and around impurity aggregates, where the free energy of the nucleus is lower than that of a nucleus on the flat surface. The above mechanisms account for the InGaN nanoring formation during initial MOCVD growth. Figure 10 shows a schematic view of the proposed mechanism, with the atoms migrating toward the mask edges to form ring structures.

By extending the growth time to 5 min, the InGaN deposit fills up the nanopores to form nanodots, as shown in Figure 9b. For even longer growth times (12 min), the InGaN starts to grow over the SiO_2 mask surface in the lateral direction (lateral overgrowth) as shown in Figure 9c. For the longer growth time, we observed the formation of nanoarrows in the cross-sectional SEM image, as shown in the inset of Figure 9c. The nanoarrows extend laterally at dimensions larger than the diameters of the SiO_2 nanopores, which is also evident in the TEM image shown in Figure 11d. Figure 11 shows cross-sectional TEM images of the individual InGaN nanostructures grown for different times. It is clear that for increasing growth times the structure evolves from a ring shape to an arrow shape. Two truncated InGaN nanopyramids, which correspond to the cross-sectional view of the nanoring structure, are observed in the TEM image (Figure 11a) inside the pores of the mask. These images indicate that the nucleation of InGaN occurs preferentially at the edges of the nanopores, which leads to the formation of the nanorings. As observed in Figure 11b, the nanorings grow laterally and vertically, leading to the coalescence at the center of the nanoring to form a faceted nanodot (shown as Figure 11c) as discussed previously. It should be pointed out that the formation of nanorings and nanodots occurs entirely inside the pores of the template. The height of the nanostructures mentioned above is lower than that of the mask. If the growth continues beyond the thickness of SiO_2 , InGaN grows laterally over the SiO_2 mask surface (shown as Figure 11d), which is similar to what is observed in normal ELO growth. The arrows have closed tips and six faces which are assigned as $\{1\bar{1}01\}$ -type facets. The faces of the arrows are assigned as the $\{1011\}$ planes, as evidenced by the angle between the inclined edge and the base of the arrow. The measured angle of $\sim 61^\circ$ is in good agreement

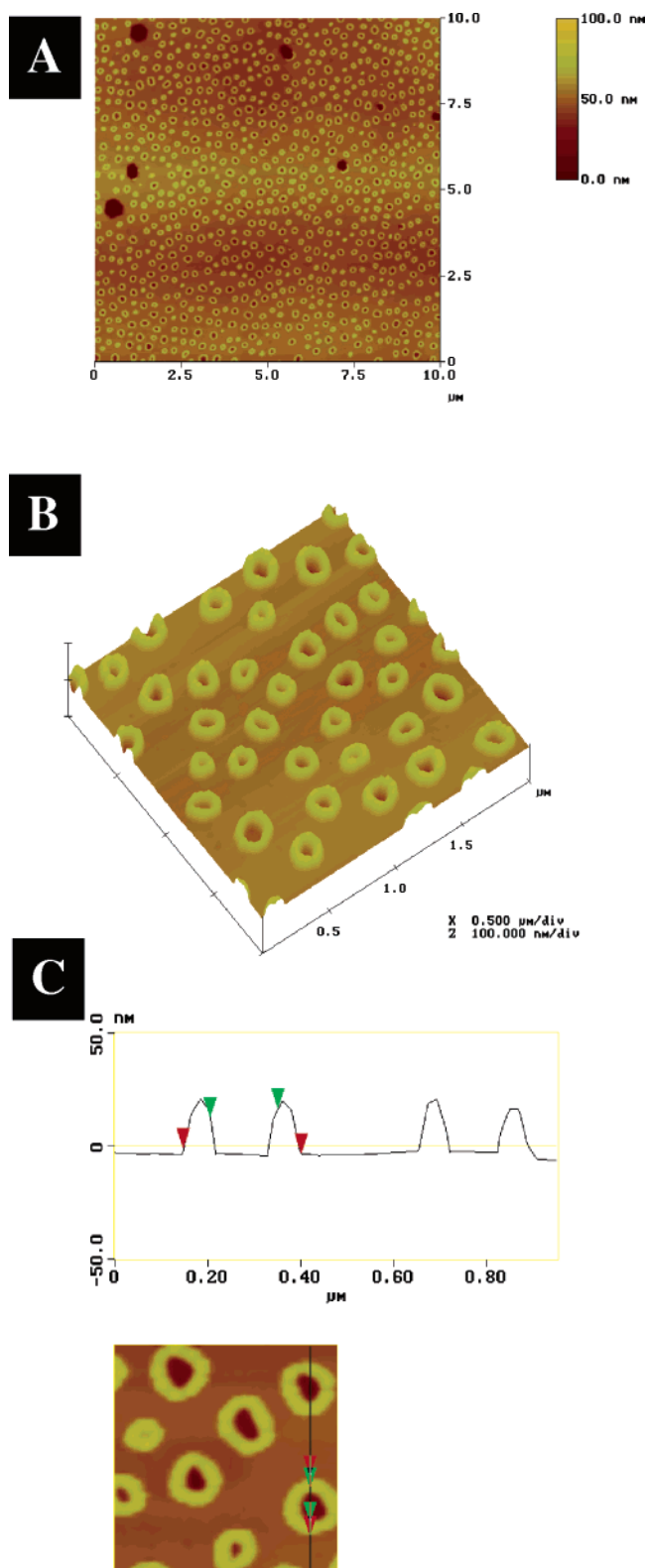


Figure 12. AFM images of InGaN nanorings: (a) top view; (b) 3D view; and (c) sectional view.

with the calculated angle of 62° for such facets. The size of the base of the InGaN arrows as well as their height depends on the growth conditions as well as the pore diameter-to-height ratios.

In addition to controlling the morphology of the nanostructures, by tuning the pore diameters and spacings in the AAO templates we can also produce nanostructure arrays with different diameters and densities. For example, by starting with

larger pores produced by anodization in 0.3 M phosphoric acid at 150 V with a 150 min pore-widening treatment, the center-to-center pore spacing and pore diameter of the AAO template are ~ 400 and 250 nm, respectively. With an InGaN growth temperature and time of 750 $^\circ\text{C}$ and 5 min, respectively, then we obtain InGaN nanoring arrays, as shown in Figure 12a. Dense InGaN nanorings are distributed uniformly across the $10\ \mu\text{m} \times 10\ \mu\text{m}$ surface. Due to the distribution of pore diameters, a small number of InGaN dots have formed in the smaller diameter pores. The hexagonal holes in the AFM image are due to pits in the underlying GaN substrate. The density of the rings is $\sim 5 \times 10^8/\text{cm}^2$, which is the same as that of the original AAO template. Panels b and c of Figure 12 show 3D and cross-section AFM images of these InGaN nanoring arrays. The outer diameter of the rings is 250 nm, which corresponds to the pore diameter in the AAO template. The inner diameter of the rings is 120 nm and the height of the rings is estimated to be 25 ± 5 nm as observed in the cross-section AFM image, both of which can be tuned by the InGaN growth duration.

4. Conclusion

In summary, we have fabricated dense arrays of InGaN nanostructures with controllable sizes and morphologies by selective area growth using nanoporous templates. The nanopores were created in a SiO_2 transfer layer by ICP etching, using anodic alumina templates as etch masks. The diameters of the resulting InGaN nanostructures ranged from 35 to 250 nm, as determined by the dimensions in the original AAO templates, which can be tuned over a wide range by controlling the anodization conditions. The mechanism of nanostructure formation is selective growth in the confined nanoscale pores. Structures evolving from nanorings to nanoarrows have been observed by controlling the growth time. Our results show that the template-assisted approach is versatile, and it may potentially be employed to fabricate other semiconductor nanostructures with well-defined size, shape, and density. In addition, this template-based approach can be extended to fabricate multi-layered nanodots and nanoheterojunction arrays.

References and Notes

- (1) Nakamura, S.; Senoh, M.; Nagahama, S.; Iwasa, N.; Yamada, T.; Matsushita, T.; Kiyoku, H.; Sugimoto, Y.; Kozaki, T.; Umenoto, H.; Sano, M.; Chocho, K. *Appl. Phys. Lett.* **1998**, *72*, 2014.
- (2) Ponce, F. A.; Bour, D. P.; *Nature* **1997**, *386*, 351.
- (3) Nakamura, S.; Fasol, G. In *The Blue Laser Diode*; Springer: New York, 1997.
- (4) Arakawa, Y.; Sakaki, H. *Appl. Phys. Lett.* **1982**, *40*, 939.
- (5) Damilano, B.; Grandjean, N.; Dalmasso, S.; Massies, J. *Appl. Phys. Lett.* **1999**, *75*, 3751.
- (6) Tanaka, S.; Iwai, S.; Aoyagi, Y. *Appl. Phys. Lett.* **1996**, *69*, 4096.
- (7) Tachibana, K.; Someya, T.; Ishida, S.; Arakawa, Y. *Appl. Phys. Lett.* **2000**, *76*, 3212.
- (8) Edwards, P. R.; Martin, R. W.; Watson, I. M.; Liu, C.; Taylor, R. A.; Rice, J. H.; Na, J. H.; Robinson, J. W.; Smith, J. D. *Appl. Phys. Lett.* **2004**, *85*, 4281.
- (9) Lee, S. C.; Stintz, A.; Brueck, S. R. J. *J. Appl. Phys.* **2002**, *91*, 3282.
- (10) Li, Q.; Han, S. M.; Brueck, S. R. J.; Hersee, S.; Jiang, Y.; Xu, H. *F. Appl. Phys. Lett.* **2003**, *83*, 5032.
- (11) Zhong, Z.; Halilovic, A.; Fromherz, T.; Schaffler, F.; Bauer, G. *Appl. Phys. Lett.* **2003**, *82*, 4779.
- (12) Lachab, M.; Nozaki, M.; Wang, J.; Ishikawa, Y.; Fareed, Q.; Wang, T.; Nishikawa, T.; Nishino, K.; Sakai, S. *J. Appl. Phys.* **2000**, *87*, 1374.
- (13) Jianyu, L.; Hope, C.; Yin, A.; Xu, J. *J. Appl. Phys.* **2002**, *91*, 2544.
- (14) Crouse, D. C.; Lo, Y. H.; Miller, A. E.; Crouse, M. *Appl. Phys. Lett.* **2000**, *76*, 49.
- (15) Masuda, H.; Yasui, K.; Nishio, K. *Adv. Mater.* **2000**, *12*, 1031.
- (16) Martin, C. R. *Chem. Mater.* **1996**, *8*, 1739.
- (17) Nielsch, K.; Muller, F.; Li, A. P.; Gosele, U. *Adv. Mater.* **2000**, *12*, 582.
- (18) Masuda, H.; Fukuda, K. *Science* **1995**, *268*, 1466.

- (19) Mei, X.; Blumin, M.; Sun, M.; Kim, D.; Wu, Z. H.; Ruda, H. E. *Appl. Phys. Lett.* **2003**, *82*, 967.
- (20) Jessensky, O.; Muller, F.; Gosele, U. *Appl. Phys. Lett.* **1998**, *72*, 1173.
- (21) Martin, C. R. *Science* **1994**, *266*, 1961.
- (22) Sander, M. S.; Tan, L. S. *Adv. Funct. Mater.* **2003**, *13*, 393.
- (23) Masuda, H.; Hasegawa, F.; Ono, S. *J. Electrochem. Soc.* **1997**, *144*, L127.
- (24) Chen, P.; Chua, S. J.; Wang, Y. D.; Sander, M. S.; Fonstad, C. G. *Appl. Phys. Lett.* **2005**, *87*, 143111.
- (25) Deb, P.; Kim, H.; Rawat, V.; Oliver, M.; Kim, S.; Marshall, M.; Stach, E.; Sands, T. *Nano. Lett.* **2005**, *5*, 1847.
- (26) Li, A. P.; Muller, F.; Birner, A.; Nielsch, K.; Gosele, U. *J. Appl. Phys.* **1998**, *84*, 6023.
- (27) Mikulskas, I.; Juodkazis, S.; Tomasiunas, R.; Dumas, J. G. *Adv. Mater.* **2001**, *13*, 1574.
- (28) Masuda, H.; Yamada, F. H.; Satoh, M.; Asoh, H.; Nakao, M.; Tamamura, T. *Appl. Phys. Lett.* **1997**, *71*, 2770.
- (29) Yu, Z. H.; Johnson, M. A. L.; McNulty, T.; Brown, J. D.; Cook, J. W.; Schetzina, J. F. *MRS Internet J. Nitride Semicond. Res.* **1998**, *3*.
- (30) Coltrin, M. E.; Willan, C. C.; Bartram, M. E.; Han, J.; Missert, N.; Crawford, M. H.; Baca, A. G. *MRS Internet J. Nitride Semicond. Res.* **1999**, *4S1*, G6.9.
- (31) Beaumont, B.; Vennegues, P.; Gibart, P. *Phys. Status Solidi B* **2001**, *227*, 1.
- (32) Zheleva, T. S.; Nam, O.; Bremser, M. D.; Davis, R. F. *Appl. Phys. Lett.* **1997**, *71*, 2472.
- (33) Li, X.; Bohn, P. W.; Kim, J.; White, J. O.; Coleman, J. J. *Appl. Phys. Lett.* **2000**, *76*, 3031.
- (34) Mei, X.; Kim, D.; Ruda, H. E.; Guo, Q. X. *Appl. Phys. Lett.* **2002**, *81*, 361.
- (35) Adelman, C.; Simon, J.; Feuillet, G.; Pelekanos, N. T.; Daudin, B.; Fishman, G. *Appl. Phys. Lett.* **2000**, *76*, 1570.
- (36) Luryi, S.; Suhir, E. *Appl. Phys. Lett.* **1986**, *49*, 140.
- (37) Alizadeh, A.; Sharma, P.; Ganti, S.; Leboeuf, S. F.; Tsakalakos, L. *J. Appl. Phys.* **2004**, *95*, 8199.
- (38) Kato, Y.; Kitamura, S.; Hiramatsu, K.; Sawaki, N. *J. Cryst. Growth* **1994**, *144*, 133.
- (39) Porter, D. H.; Easterling, K. E. In *Phase Transformations in Metals and Alloys*. Chapman & Hall: New York, 1992.